Study of non-axisymmetric divertor footprints using 2-D IR and visible cameras and a 3-D heat conduction solver in NSTX

J-W. Ahn [a],[*],[1], K.F. Gan [b], F. Scotti [c], J.D. Lore [a], R. Maingi [a], J.M. Canik [a], T.K. Gray [a], A.G. McLean [d], A.L. Roquemore [c], V.A. Soukhanovskii [d]

[a] Oak Ridge National Laboratory, Oak Ridge, TN 37831, USA
[b] Institute of Plasma Physics, Chinese Academy of Sciences, Hefei, People's Republic of China
[c] Princeton Plasma Physics Laboratory, Princeton, NJ 08543, USA
[d] Lawrence Livermore National Laboratory, Livermore, CA 94551, USA

ARTICLE INFO

Article history:
Available online xxxx

ABSTRACT

Toroidally non-axisymmetric divertor profiles during the 3-D field application and for ELMs are studied with simultaneous observation by a new wide angle visible camera and a high speed IR camera. A newly implemented 3-D heat conduction code, TACO, is used to obtain divertor heat flux. The wide angle camera data confirmed the previously reported result on the validity of vacuum field line tracing on the prediction of split strike point pattern by 3-D fields as well as the phase locking of ELM heat flux to the 3-D fields. TACO calculates the 2-D heat flux distribution allowing assessment of toroidal asymmetry of peak heat flux and heat flux width. The degree of asymmetry (ε_{DA}) is defined to quantify the asymmetric heat deposition on the divertor surface and is found to have a strong positive dependence on peak heat flux.

Published by Elsevier B.V.

1. Introduction

Recent studies show that the axisymmetry of divertor flux profiles can be broken in the case of applying 3-D magnetic perturbations [1–4] as well as during the ELMs [5]. In these studies, the use of 2-D infrared (IR) camera plays a vital role in obtaining surface temperature data and for the derivation of heat flux profiles. However, there are two caveats in this approach to study asymmetric divertor flux profiles. First, the viewing extent of the IR camera is often limited and therefore covers only a relatively small fraction of the full toroidal angle (Φ) unless there are more cameras at other toroidal locations. Second, heat conduction equation solvers for the calculation of divertor heat flux profile, such as THEODOR [6], are usually in 2-D, i.e. 1-D in the direction of the tile depth, and 1-D along the radial extent of the plasma facing surface. The obtained heat flux profile is therefore only 1-D, i.e. in the radial direction (r) chosen at a particular toroidal location. These two caveats significantly restrict the capability of investigating toroidal asymmetry in the divertor flux profiles. For example, one can only compare the measured heat flux profile to that from modeling for a limited range of toroidal angles. The first caveat can be overcome by the use of a wide angle camera. This is especially feasible in the compact geometry of a spherical tokamak (ST). Furthermore,

the use of a 3-D heat conduction solver can provide the capability of calculating heat flux profile for the full 2-D plane.

Two wide angle visible cameras were installed on NSTX in 2010 to provide full toroidal and radial coverage of the divertor surface [7]. 2-D images from them have been used to study the effect of applied 3-D fields and ELMs on the divertor flux profiles, with temporal resolution of 10 kHz. However, the view of the 2-D IR camera is not as wide as the one by the visible camera. The frame size is dependent on the choice of frame speed (higher frame speed lowers the frame size). Also, the toroidal extent covered by a frame size differs with radial position (a wider toroidal coverage is possible for a smaller radial location, see Fig. 1c). For the dataset in this paper, maximum of $\sim20°$ of toroidal extent was achieved with 6.3 kHz of frame speed. We also implemented a 3-D heat conduction solver, TACO [8], to obtain 2-D heat flux profiles including the effects of thin surface films on the heat flux calculation [9].

2. Experimental setup

Experiments were conducted in ELM-free and ELMy H-mode plasmas. The toroidal magnetic field (B_t) at the magnetic axis was fixed at ~0.4 T, and the neutral beam injected power (P_{NBI}) of 2–5 MW was used. Plasmas were highly shaped (elongation $\kappa \sim 2.0$–2.4, triangularity $\delta \sim 0.5$–0.8), and the plasma current was 600–800 kA. The equilibrium was maintained as a lower single-null with the direction of the B-field was for the ion ∇B drift to move towards the primary X-point. Fig. 1a shows the poloidal
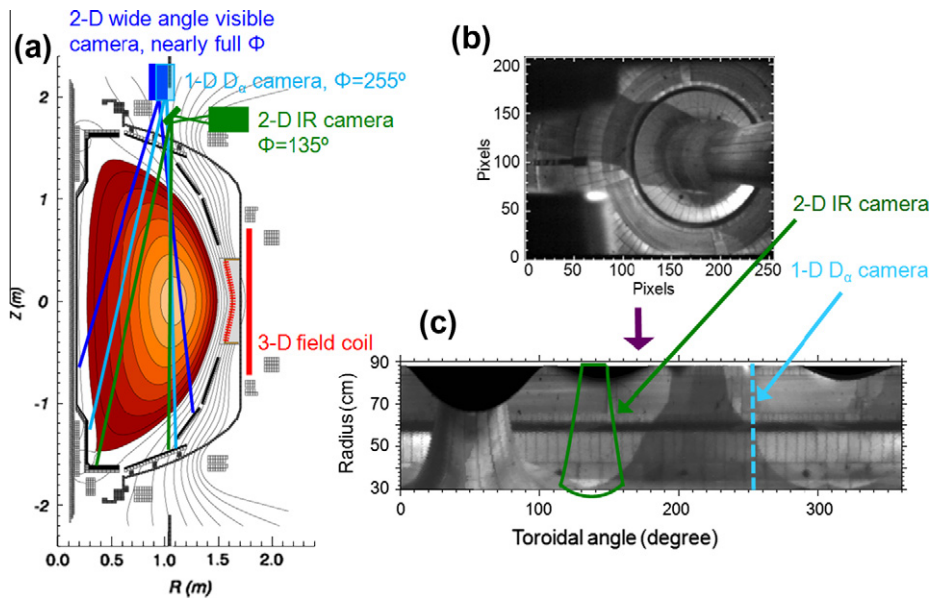
Fig. 1. Poloidal cross section of NSTX (a) with magnetic equilibrium reconstruction, field of view of the IR, D_α, and wide angle visible cameras and the location of external 3D field coil overlaid. (b) The raw image of lower divertor plates viewed by the wide angle visible camera, which is remapped to the (r, Φ) plane as in (c).

cross section of NSTX showing the location of diagnostic views as well as the external 3-D field coils. 3-D field pulses in NSTX are applied using a midplane coil set. In the experiments discussed here, these coils have been configured to apply $n = 1$ or $n = 3$ perturbative magnetic fields. The coil current was maintained at $I_{3-D} = 0.5$ kA, which is lower than the ELM triggering level, resulting in $\delta B/B \sim 0.05\%$ for the integrated δB over the coil surface. Fig. 1b shows the image of lower divertor plates viewed by the wide angle visible camera and Fig. 1c is the remapped image to the (r, Φ) plane with the spatial coverage of the IR and D_α cameras overlaid.

3. Divertor footprints during the 3-D field application

3.1. Measured heat flux profiles and comparison with wide angle images

Fig. 2a shows the radial heat flux profile measured at the toroidal location indicated by the vertical line at $\Phi \sim 135°$ in Fig. 2b, during the application of the $n = 1$ 3-D field. The wide angle visible camera used LiI filter ($\lambda = 670.9$ nm) which has been found to best resolve fine structures at the divertor surface. The remapped wide angle visible image Fig. 2b, clearly shows the asymmetric divertor footprint and the local peak at $r \sim 46$ cm in the heat flux profile, representing one of the split strike points induced by the $n = 1$

perturbation fields. Computed vacuum field line tracing was performed to obtain connection lengths (L_c) on the divertor surface and to compare the result to the wide angle camera images. Fig. 2c shows that the agreement with the image data is excellent; the radial and toroidal variation of L_c well represents the observed spatial distribution of LiI emissivity in Fig. 2b. This data confirms the conclusion of previous works [3,4] that the vacuum field line tracing reproduces the divertor footprints well in NSTX.

3.2. Divertor footprints during the ELMs triggered by 3-D field application

One of the other primary observations for the divertor footprints during 3-D field application is that the heat flux profile from ELMs triggered by applied 3-D fields follows the imposed field structure [2,10]. That is, the spatial heat deposition during the triggered ELMs is 'phase locked' to the external 3-D fields. By applying the remapping technique of wide angle images for the divertor footprints of the triggered ELMs, the phase locking is also reconfirmed for both $n = 1$ and $n = 3$. Fig. 3 illustrates the agreement between images before and during an ELM with $n = 1$ applied. It is shown that the structure of asymmetric divertor footprint before the ELM is maintained during the ELM even with significantly
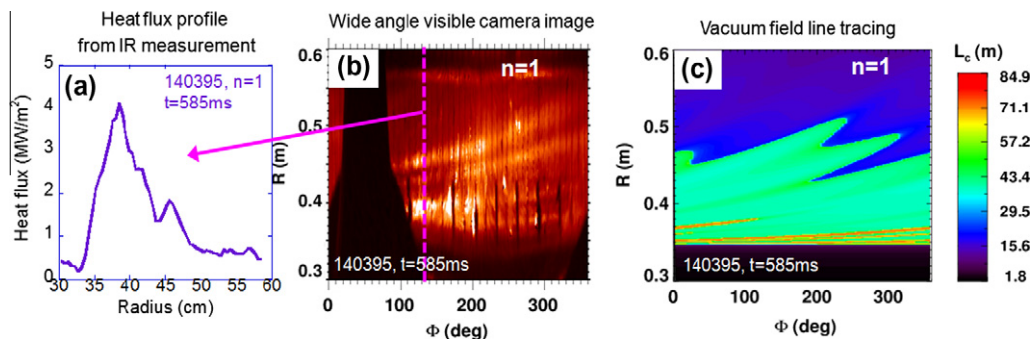

Fig. 2. Comparison of 1-D heat flux profile from the IR measurement (a) with the remapped 2-D wide angle visible camera image using a LiI filter ($\lambda = 670.9$ nm) (b), during the $n = 1$ magnetic perturbation. (c) The contour plot of calculated connection lengths for the same time slice.
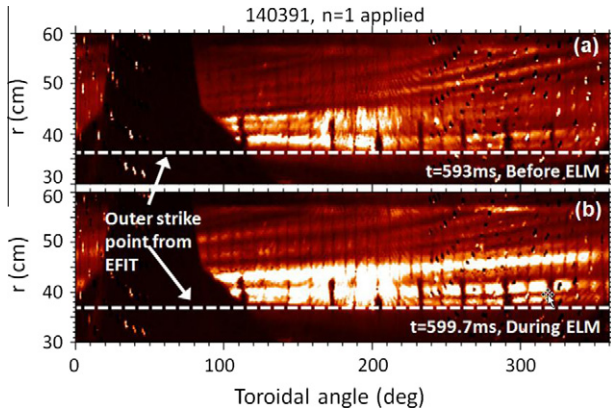
Fig. 3. Images of wide angle visible camera for lower divertor plates during the $n = 1$ 3-D field application, remapped from (x,y) to (r,Φ) plane. The upper image is before the ELM and the lower one is during the ELM, triggered by $n = 1$ magnetic perturbation. The light intensity for the ELM case (lower image) was reduced for clearer comparison.

stronger emission intensity. Note that the emission intensity for Fig. 3b was reduced to the level of 3a for a more direct comparison.

4. Analysis of asymmetric divertor heat flux for ELMy plasmas with no 3-D field application

4.1. TACO 3-D heat conduction solver

TACO has been implemented for use on NSTX to calculate heat flux at the divertor surface for full 2-D plane. This provides a significant advantage over a 1-D radial profile particularly in the study of toroidal distribution of heat deposition. We also incorporated the thin surface film correction applied in THEODOR [6] into the process of solving heat conduction equation [9] by introducing a heat transmission coefficient, α. Various α values have been tested and temporal behavior of the estimated energy deposition after the end of discharge (*i.e.*, when the heat deposited on the surface by the plasma is removed) is found to be different for different α values. Higher α values lead to the decrease of the deposited energy, while lower ones cause it to increase, after the end of discharge. Therefore an α value of 60 kW m^{-2} K^{-1} was chosen to keep the energy deposition constant and this is believed to best account for poor surface layer adhesion to the tile substrate for the dataset in this study [9]. This value was used for all analysis presented in this

paper. We have compared the 2-D heat distribution data from TACO to the 1-D radial profile data from THEODOR, (*i.e.* by obtaining a 1-D radial profile from the 2-D TACO data at the same toroidal location as in the THEODOR calculation), and the two results are quite similar. We suspect this may be due to the relatively short pulse length (usually ⩽0.5 s) for the dataset used in this paper, so that it may not have had sufficient time for the heat transport in the toroidal direction to make a significant difference.

The 2-D heat flux data calculated by TACO was remapped to r and Φ, as was done for the wide angle visible images. Fig. 4 shows an example of the measured 2-D surface temperature and the computed 2-D heat flux profile from TACO, as well as the remapped image of the heat flux from (x,y) to the (r,Φ) plane. This allowed for the evaluation of peak heat flux q_{peak} and heat flux width λ_q for each toroidal angle, which in turn generates a toroidal array of these quantities at each time slice. Here, we used the definition of integral λ_q used in [11], i.e. $\lambda_q = P_{div}/(2\pi r_{peak}^{div} q_{peak}^{div})$.

4.2. Toroidal asymmetries in peak heat flux and heat flux width

In order to quantify how asymmetric the toroidal distribution of q_{peak} and λ_q is, the toroidal degree of asymmetry (ε_{DA}) for q_{peak} and λ_q, representing the full 2-D plane monitored by the IR camera, as a function of time was defined as $\varepsilon_{DA}(q_{peak}) = \sigma_{peak}/\bar{q}_{peak}$ and $\varepsilon_{DA}(\lambda_q) = \sigma_{\lambda q}/\bar{\lambda}_q$. Here, σ is the standard deviation of q_{peak} and λ_q over data in the toroidal array. This value is normalized by mean values of q_{peak} and λ_q respectively to produce an ε_{DA} value at each time slice. Here, $\bar{q}_{peak}$ and $\bar{\lambda}_q$ is the average over values along the toroidal direction. In case of ELMs, the helical heat deposition produces strong toroidal asymmetry for both q_{peak} and λ_q and therefore generates additional scatter of data around the mean value to the background scatter level. The raw data have been also examined to check if the tile gaps have caused errors on ε_{DA} values, and we confirmed that they did not make a major contribution to the evolution of ε_{DA} for the dataset presented in this paper.

An example of temporal evolution of $\bar{q}_{peak}$ and $\bar{\lambda}_q$ for a type-III ELMy discharge, with no 3-D field application, is given in Fig. 5a. Note that $\bar{\lambda}_q$ drops during the ELMs while $\bar{q}_{peak}$ jumps. Although the decrease of λ_q during the ELM is opposite to the modest ELM broadening of heat flux width (1–2 times that of inter-ELM period) reported from some other machines [12,13], the deposited ELM power rapidly increases and peaks at the same time as that for the peak heat flux. Fig. 5b shows the temporal evolution of ε_{DA} for both q_{peak} and λ_q and it is seen that both asymmetries jump with the rise of peak heat flux. It is interesting to note that $\varepsilon_{DA}(\lambda_q)$ increases during the ELM even though λ_q itself decreases.
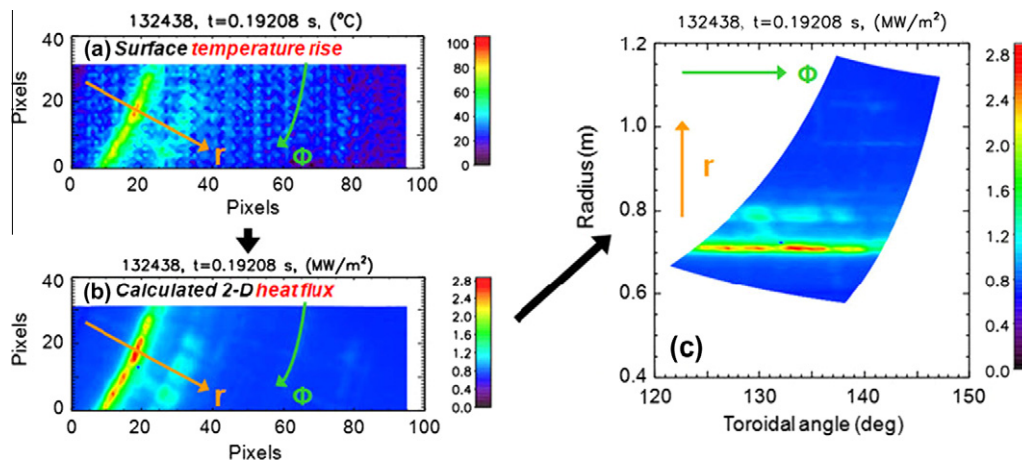

Fig. 4. (a) Measured 2-D surface temperature, (b) calculated 2-D heat flux profile from TACO, and (c) remapped 2-D heat flux profile from (x,y) to (r,Φ) plane.
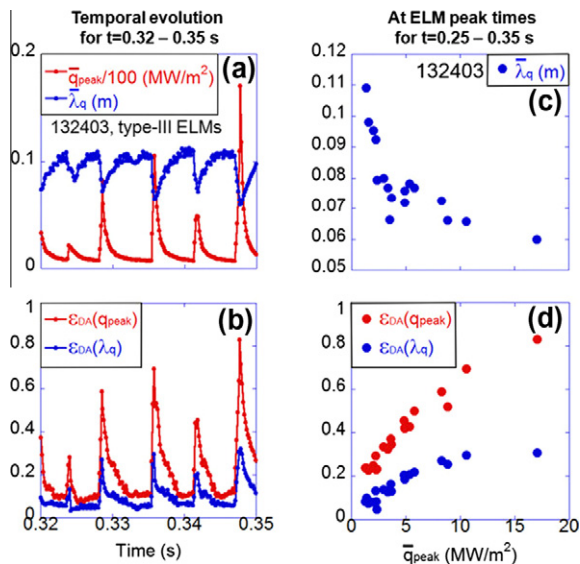
Fig. 5. Temporal evolution of mean q_{peak} and λ_q (a) as well as of ε_{DA} for each quantity (b). (c) and (d) The dependence of average λ_q and ε_{DA}, respectively, on q_{peak}.

Probing dependence of parameters on the peak heat flux value at ELM peak times revealed that heat flux width decreases with increasing peak heat flux (see Fig. 5c). On the other hand, ε_{DA} for q_{peak} and λ_q increases with increasing $\bar{q}_{peak,ELM}$, although the rate of increase slows down with rising $\bar{q}_{peak,ELM}$. The absolute value of $\varepsilon_{DA}(q_{peak})$ is always greater than $\varepsilon_{DA}(\lambda_q)$ and the ratio $\varepsilon_{DA}(q_{peak})/\varepsilon_{DA}(\lambda_q)$ is typically ∼2–3.

The dependence of the ε_{DA} on the period within an ELM cycle was also investigated for type-I ELMy H-mode. It is found that the dependence of both $\varepsilon_{DA}(q_{peak})$ and $\varepsilon_{DA}(\lambda_q)$ on $\bar{q}_{peak}$ is similar to the case of type-III ELMs. That is, they become largest at the ELM peak times and $\varepsilon_{DA}(q_{peak})$ can be as high as ∼1.4 while $\varepsilon_{DA}(\lambda_q)$ can reach up to ∼0.5 for the dataset examined. Both ε_{DA} values increase with increasing q_{peak} and therefore the degree of asymmetric heat deposition is highest at the ELM peak times, while it becomes lower toward the later stage of the inter-ELM period. This dependence of asymmetric heat deposition on the ELM cycle also appears to be related to the absolute value of peak heat flux. That is, higher peak heat flux leads to stronger degree of asymmetric q_{peak} and λ_q. It is also found that the correlation between $\varepsilon_{DA}(q_{peak})$ and $\varepsilon_{DA}(\lambda_q)$ is the strongest at ELM peak times and becomes weaker later in the ELM cycle.

5. Discussion and summary

The study of divertor heat and particle deposition can be more comprehensively carried out by making use of 2-D image diagnostics. The compact ST geometry of NSTX makes the coverage of toroidal extent almost full by a single wide angle visible camera and this turns out very effective to investigate divertor footprint patterns during the 3-D field application or ELMs.

While the present NSTX fast IR camera does not provide toroidal coverage approaching that of the visible cameras, the view is significantly wider than similar instruments on conventional tokamaks with comparable frame speeds. TACO can directly produce 2-D heat flux data and this has been used to study toroidal asymmetry of heat flux. The degree of asymmetry ε_{DA} was defined here to quantify how asymmetrically q_{peak} and λ_q are distributed over the whole monitored divertor surface at a given time slice. The choice of $\alpha = 60$ kW m^{-2} K^{-1} is based on the energy conservation and alleviates the negative heat flux problem that occurs when not considering the effect of surface layers in solving the heat conduction equation. The rapid increase of ε_{DA} during the ELM reflects that ELMs make divertor heat deposition highly asymmetric compared to the inter-ELM period. A possible explanation for the fact that ε_{DA} becomes larger with increasing size of ELMs (i.e. with increasing q_{peak} at ELM peak times) is that bigger ELMs would deposit higher toroidally localized heat fluxes and therefore increase the toroidal asymmetry in heat flux. Contribution of tile gaps and misalignments to the temporal evolution of ε_{DA} in the ELMy phase is negligible for the dataset in this paper. The relatively narrow view of the IR camera compared to that of the fast visible camera naturally poses a limit in capturing the asymmetry with wavelength longer than the maximum length of toroidal coverage. The use of integral λ_q, instead of the decay length from the exponential fitting, is believed to better represent the heat flux width because the radial heat flux profile is often modified from the exponential decay pattern by the presence of ELM filaments as well as the strike point splitting by applied 3-D fields.

References

[1] O. Schmitz, T.E. Evans, M.E. Fenstermacher, et al., Plasma Phys. Control. Fusion 50 (2008) 124029.
[2] M.W. Jakubowski, T.E. Evans, M.E. Fenstermacher, et al., Nucl. Fusion 49 (2009) 095013.
[3] J.-W. Ahn, J.M. Canik, V.A. Soukhanovskii, et al., Nucl. Fusion 50 (2010) 045010.
[4] J.-W. Ahn, R. Maingi, J.M. Canik, et al., Phys. Plasmas 18 (2011) 056108.
[5] T. Eich, A. Herrmann, J. Neuhauser, et al., Plasma Phys. Control. Fusion 47 (2005) 815.
[6] A. Herrmann, W. Junker, K. Günther, et al., Plasma Phys. Control. Fusion 37 (1995) 17.
[7] F. Scotti, A.L. Roquemore, V.A. Soukhanovskii, Rev. Sci. Instrum. 83 (2012) 10E532.
[8] G. Castle, Theory and Operating Instructions for the taco_run Code", COMPASS Note 97.16, UKAEA Fusion, 1997.
[9] K.F. Gan, J-W. Ahn, J.-W. Park, et al., 2D divertor heat flux distribution using a 3D heat conduction solver in NSTX, Rev. Sci. Instum. (2013), in press.
[10] J.-W. Ahn, J.M. Canik, R. Maingi, et al., J. Nucl. Mater. 415 (2011) S918.
[11] A. Loarte, S. Bosch, A. Chankin, et al., J. Nucl. Mater. 266–269 (1999) 587.
[12] A. Herrmann, T. Eich, S. Jachmich, et al., J. Nucl. Mater. 313–316 (2003) 759.
[13] A.W. Leonard, A. Herrmann, K. Itami, et al., J. Nucl. Mater. 266–269 (1999) 109.